



A model for the dissipation rate in linear unsteady flow through porous media

Lukas Unglehart^{1,†} and Michael Manhart¹

¹Professorship of Hydromechanics, Technical University of Munich, Arcisstr. 21, 80333 Munich, Germany

(Received 30 June 2023; revised 24 August 2023; accepted 16 October 2023)

We present a model for the volume-averaged dissipation rate in linear unsteady flow through porous media. The model is derived by blending a new small-time asymptotic expression for the dissipation rate obtained from boundary layer theory with the known large-time asymptotic expression obtained from Darcy's law. The resulting model is a second-order Volterra functional of the volume-averaged acceleration. We validate the model with an analytical solution for transient flow through a porous medium composed of circular tubes and with numerical simulations of transient and oscillatory flow through a cylinder array and through a hexagonal sphere pack.

Key words: porous media

1. Introduction

The theory of unsteady flow through porous media can be applied to a variety of different systems. For example, it can be used to describe wave-induced flow through the seabed (Gu & Wang 1991) or coral reefs (Lowe *et al.* 2008) or the propagation of acoustic and seismic waves through the Earth (Biot 1956*a,b*). Furthermore, Cha *et al.* (2007) modelled endovascular coil embolisation, a treatment for aneurysms, as a porous medium interacting with the blood flow. In engineering applications, unsteady flow through porous media can be used to describe regenerator-type heat exchangers (Trevizoli, Peixer & Barbosa 2016) or pulsed flow in chemical reactors (Ni *et al.* 2003).

Using the volume-averaging framework (Whitaker 1966, 1986) or homogenisation theory (Ene & Sanchez-Palencia 1975), a macroscopic description of flow through porous media can be derived from the Navier–Stokes equations. The macroscopic variables are

† Email address for correspondence: lukas.unglehart@tum.de

the superficial velocity, which is defined as

$$\langle \mathbf{u} \rangle_s = \frac{1}{V} \int_{V_f} \mathbf{u} \, dV, \tag{1.1}$$

and the intrinsic pressure, which is defined as

$$\langle p \rangle_i = \frac{1}{V_f} \int_{V_f} p \, dV, \tag{1.2}$$

where V_f is the volume of fluid contained in the representative volume element or unit cell, which has a combined solid and fluid volume V . The volume averaging gives rise to effective properties of the porous medium, such as the porosity ϵ , which is defined as the ratio V_f/V , and the permeability K , which relates $\langle \mathbf{u} \rangle_s$ and $\nabla \langle p \rangle_i$ by Darcy’s law $\langle \mathbf{u} \rangle_s = K/\mu \nabla \langle p \rangle_i$ (Darcy 1856).

Accurate models exist for the superficial velocity in linear flow (Johnson, Koplik & Dashen 1987; Chapman & Higdon 1992; Pride, Morgan & Gangi 1993), which allow the superficial velocity to be calculated in response to an arbitrary forcing. On the other hand, there is no comparably general model for the volume-averaged dissipation rate. Knowledge of the volume-averaged dissipation rate as a functional of the superficial velocity allows computation of the volume-averaged kinetic energy $\langle k \rangle_s = \left\langle \frac{1}{2} \rho \mathbf{u}^2 \right\rangle_s$ using the equation (Zhu *et al.* 2014)

$$\frac{d\langle k \rangle_s}{dt} = - \langle \mathbf{u} \rangle_s \cdot \nabla \langle p \rangle_i - 2\mu \langle \mathbf{S} : \mathbf{S} \rangle_s, \tag{1.3}$$

where ρ is the density, μ is the dynamic viscosity and \mathbf{S} is the strain rate tensor. The volume-averaged kinetic energy and dissipation rate could be used to model scalar transport in unsteady flow. For instance, the small-time asymptotic descriptions of the dispersion coefficient and the temporal velocity autocorrelation function require knowledge of the volume-averaged kinetic energy and dissipation rate (Brosten 2013, (6.10) and (6.14)). Also, the continuous time random walk description of dispersion involves the volume-averaged kinetic energy of the Stokes flow (Cortis *et al.* 2004, (7) and (8)).

The volume-averaged dissipation rate in a steady linear flow has been given, for example, by Murthy & Singh (1997) or Zhu *et al.* (2014) as

$$2\mu \langle \mathbf{S} : \mathbf{S} \rangle_s = \frac{\mu}{K} \langle \mathbf{u} \rangle_s^2, \tag{1.4}$$

which was derived by equating the dissipation rate to the power input into the flow and then using Darcy’s law. This expression was confirmed by Paéz-García, Valdés-Parada & Lasseux (2017), who applied an upscaling procedure to the mechanical energy equation. On the other hand, no comparable equation has been given for the volume-averaged dissipation rate in unsteady linear flow. A difficulty in modelling the dissipation rate arises from its nonlinear dependence on the velocity field. Thus, unlike the superficial velocity, the dissipation rate therefore cannot be obtained from a superposition of single-frequency modes (for which the dissipation rate has been computed, for example, by Johnson *et al.* (1987)).

In this paper, we present a time domain model for the volume-averaged dissipation rate in linear unsteady flow. The model is derived by blending the steady-state dissipation rate (1.4) with the small-time limit of the dissipation rate obtained from boundary layer theory. The model is validated with an analytical solution of transient flow through a bundle of

circular tubes and with direct numerical simulations (DNS) of flow through a periodic cylinder array and a periodic sphere pack.

2. Derivation of the model

2.1. Boundary layer theory

In this section, we derive a new asymptotic expression for the volume-averaged dissipation rate in linear flow that is valid in the small-time or high-frequency limits. Under these circumstances, the local acceleration term of the unsteady Stokes equation is dominant compared with the viscous term and the flow is laminar and has a boundary layer structure (Schlichting & Gersten 2017, pp. 349–350).

For the sake of this derivation, we assume that the flow is at rest at $t = 0$ and that the macroscopic pressure gradient is applied for $t \geq 0$. Then, for small times, the flow can be approximated as a potential core flow and a viscous boundary layer flow (Schlichting & Gersten 2017, pp. 352–353) and the velocity profile in the boundary layer is locally given by the solution to Stokes' first problem (Schlichting & Gersten 2017, pp. 126–128)

$$\mathbf{u}(y, t) = \int_0^t \frac{\partial \mathbf{U}}{\partial \tau} \Big|_{y=0} \operatorname{erf}\left(\frac{y}{2\sqrt{\nu(t-\tau)}}\right) d\tau. \quad (2.1)$$

Here, $\nu = \mu/\rho$ is the kinematic viscosity and y is the local wall-normal coordinate. The velocity of the potential core flow $\mathbf{U}(\mathbf{x}, t)$ can be obtained from the theory of unsteady potential flow (Batchelor 2000, pp. 394–409) for a given pore geometry. As will be discussed below, $\mathbf{U}(\mathbf{x}, t)$ enters the volume-averaged dissipation rate only through the two integral quantities α_∞ and Λ (2.6), which have been tabulated for simple geometries (Chapman & Higdon 1992; Lee, Leamy & Nadler 2009). The volume-averaged dissipation rate is equal to the sum of the dissipation in the boundary layer and the dissipation in the potential core flow (Johnson *et al.* 1987),

$$2\mu \langle \mathbf{S} : \mathbf{S} \rangle_s = \underbrace{\frac{\mu}{V} \int_{A_{fs}} \int_0^\infty \left(\frac{\partial \mathbf{u}}{\partial y}\right)^2 dy dA}_{\text{boundary layer}} + \underbrace{\frac{\mu}{V} \int_{A_{fs}} \nabla |\mathbf{U}|^2 \cdot \mathbf{n} dA}_{\text{potential flow } (\approx 0)}, \quad (2.2)$$

where A_{fs} denotes the fluid–solid interface. As observed by Johnson *et al.* (1987), the boundary layer term increases with frequency whereas the potential flow term is independent of frequency and can be neglected. In the boundary layer contribution, we can identify the dissipation integral

$$D = \int_0^\infty \left(\frac{\partial \mathbf{u}}{\partial y}\right)^2 dy = \int_0^\infty \left[\int_0^t \frac{\partial \mathbf{U}}{\partial \tau} \Big|_{y=0} \exp\left(-\frac{y^2}{4\nu(t-\tau)}\right) \frac{1}{\sqrt{\pi\nu(t-\tau)}} d\tau \right]^2 dy. \quad (2.3)$$

Here, we have departed from Johnson *et al.* (1987) in pursuing a time-domain approach. Now, we change the order of spatial and temporal integration. With the integral

$$\int_0^\infty \exp\left(-\frac{y^2}{4\nu(t-\tau_1)}\right) \exp\left(-\frac{y^2}{4\nu(t-\tau_2)}\right) dy = \sqrt{\frac{\pi\nu(t-\tau_1)(t-\tau_2)}{(t-\tau_1) + (t-\tau_2)}}, \quad (2.4)$$

we can rewrite the dissipation integral as a double convolution,

$$D = \int_0^t \int_0^t \frac{\partial \mathbf{U}}{\partial \tau_1} \Big|_{y=0} \frac{\partial \mathbf{U}}{\partial \tau_2} \Big|_{y=0} \frac{1}{\sqrt{\pi\nu[(t-\tau_1) + (t-\tau_2)]}} d\tau_1 d\tau_2. \quad (2.5)$$

The spatial integration has thus changed the square of a one-dimensional convolution integral into a two-dimensional convolution integral. For the potential flow, there is a time-independent proportionality between the potential flow velocity at the wall $U|_{y=0}$ and the superficial velocity $\langle U \rangle_s$ of the potential flow. This relationship is expressed by the high-frequency limit of the dynamic tortuosity α_∞ and the characteristic viscous length Λ derived by Johnson *et al.* (1987):

$$\frac{\alpha_\infty}{\epsilon} = \frac{\langle U^2 \rangle_s}{\langle U \rangle_s^2}, \tag{2.6a}$$

$$\frac{2}{\Lambda} = \frac{\frac{1}{V} \int_{A_{fs}} |U|^2 \, dA}{\langle U^2 \rangle_s}. \tag{2.6b}$$

Using these expressions, the surface integral over the dissipation integral in (2.2) can be rewritten in terms of the superficial velocity of the potential flow. Furthermore, the superficial velocity of the potential flow can be approximated with the actual superficial velocity provided that the boundary layer is very thin. This gives the final expression for the volume-averaged dissipation rate in the small-time limit

$$2\mu \langle \mathbf{S} : \mathbf{S} \rangle_s = \frac{2\mu\alpha_\infty}{\epsilon\Lambda} \int_0^t \int_0^t \frac{d\langle \mathbf{u} \rangle_s}{d\tau_1} \cdot \frac{d\langle \mathbf{u} \rangle_s}{d\tau_2} \frac{1}{\sqrt{\pi\nu [(t - \tau_1) + (t - \tau_2)]}} \, d\tau_1 \, d\tau_2, \tag{2.7}$$

which is a key result of this study.

2.2. Blending of steady and boundary layer asymptotics

In this section, we use the expressions for the volume-averaged dissipation rate for small times (2.7) and for the steady state (1.4) to construct a model for the volume-averaged dissipation rate that is valid for linear flow.

We begin by rewriting the steady-state dissipation rate (1.4) as a second-order Volterra integral similar to (2.7):

$$2\mu \langle \mathbf{S} : \mathbf{S} \rangle_s = \frac{\mu}{K} \langle \mathbf{u} \rangle_s^2 = \frac{\mu}{K} \int_0^t \int_0^t \frac{d\langle \mathbf{u} \rangle_s}{d\tau_1} \cdot \frac{d\langle \mathbf{u} \rangle_s}{d\tau_2} \, d\tau_1 \, d\tau_2. \tag{2.8}$$

This leads us to consider a general model for the dissipation rate in the linear regime of the following form:

$$2\mu \langle \mathbf{S} : \mathbf{S} \rangle_s = \int_0^t \int_0^t \frac{d\langle \mathbf{u} \rangle_s}{d\tau_1} \cdot \frac{d\langle \mathbf{u} \rangle_s}{d\tau_2} g(t - \tau_1, t - \tau_2) \, d\tau_1 \, d\tau_2, \tag{2.9}$$

where the kernel function $g(t_1, t_2)$ is assumed to be symmetric, $g(t_1, t_2) = g(t_2, t_1)$, and satisfies the limits

$$\lim_{t_1 \rightarrow 0} \lim_{t_2 \rightarrow 0} g(t_1, t_2) = \frac{2\mu\alpha_\infty}{\epsilon\Lambda} \frac{1}{\sqrt{\pi\nu [t_1 + t_2]}}, \tag{2.10a}$$

$$\lim_{t_1 \rightarrow \infty} \lim_{t_2 \rightarrow \infty} g(t_1, t_2) = \frac{\mu}{K}. \tag{2.10b}$$

The latter condition can be explained as follows: for a function that varies very slowly, only a small part of the history will be affected by the small-time limit of $g(t_1, t_2)$, while most of the history will be weighted with μ/K , thus approaching the steady-state limit.

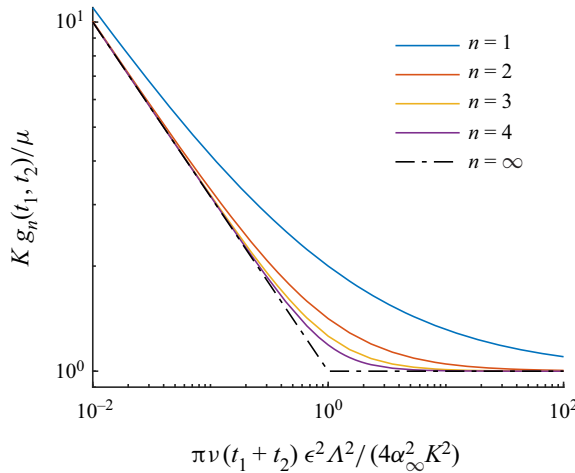


Figure 1. Kernel function $g_n(t_1, t_2)$ for different values of the blending parameter n in logarithmic axes. The kernel function is universal in the chosen normalisation.

Following Churchill & Usagi (1972), we consider the following family of models:

$$g_n(t_1, t_2) = \left[\left(\frac{\mu}{K} \right)^n + \left(\frac{2\mu\alpha_\infty}{\epsilon\Lambda} \frac{1}{\sqrt{\pi\nu[t_1 + t_2]}} \right)^n \right]^{1/n}, \quad (2.11)$$

where n is a real number. In this blending, the transition between the small- and large-time behaviour occurs when the limiting expressions (2.10) take the same value. The family parameter n could be determined using additional information about the dissipation rate. Here, the parameter will be estimated empirically based on analytical solutions and numerical simulations. Figure 1 shows the kernel function (2.11) for different values of the parameter n . It can be seen that the width of the transition region between the asymptotes decreases with increasing values of n .

In the remainder of this paper, the proposed model is validated using analytical and numerical solutions to the (Navier–)Stokes equations for unsteady flow through porous media.

3. Analytical validation

In this section, we validate the model for the case of transient flow through a porous medium consisting of cylindrical tubes of radius R that are inclined by an angle θ with respect to the pressure gradient. Johnson *et al.* (1987) reported the exact values for the permeability, the high-frequency limit of the dynamic tortuosity and the characteristic viscous length for this case,

$$K = \frac{1}{8} \epsilon R^2 \cos^2 \theta, \quad (3.1a)$$

$$\alpha_\infty = \frac{1}{\cos^2 \theta}, \quad (3.1b)$$

$$\Lambda = R. \quad (3.1c)$$

In the following, we show that the volume-averaged dissipation rate obtained from the analytical solution agrees with the asymptotic limits (2.7) and (1.4) and we compare our proposed model (2.11) for the volume-averaged dissipation rate with the exact solution.

3.1. *Exact solution for the dissipation rate*

The analytical solution for the streamwise velocity in transient flow through a circular pipe is given as (Pozrikidis 2017, pp. 509–514)

$$u_s(r, t) = \frac{1}{4\mu} |\nabla\langle p\rangle_i| \cos\theta \left[R^2 - r^2 - 8R^2 \sum_{k=1}^{\infty} \frac{1}{\alpha_k^3} \frac{J_0(\alpha_k r/R)}{J_1(\alpha_k)} \exp\left(-\alpha_k^2 \frac{\nu t}{R^2}\right) \right], \quad (3.2)$$

where $J_n(z)$ are the Bessel functions of the first kind and α_k denotes the k th zero of the Bessel function J_0 . The velocity gradient can be calculated as

$$\frac{\partial u_s}{\partial r} = \frac{1}{4\mu} |\nabla\langle p\rangle_i| \cos\theta \left[-2r + 8R \sum_{k=1}^{\infty} \frac{1}{\alpha_k^2} \frac{J_1(\alpha_k r/R)}{J_1(\alpha_k)} \exp\left(-\alpha_k^2 \frac{\nu t}{R^2}\right) \right]. \quad (3.3)$$

We can then obtain the superficial volume-averaged dissipation rate by integration as

$$\begin{aligned} 2\mu \langle \mathbf{S} : \mathbf{S} \rangle_s &= \frac{\epsilon\mu}{\pi R^2} \int_0^R \left(\frac{\partial u_s}{\partial r} \right)^2 2\pi r \, dr \\ &= \frac{1}{8\mu} \epsilon R^2 \cos^2\theta |\nabla\langle p\rangle_i|^2 \int_0^1 \left[-2x + 8 \sum_{k=1}^{\infty} \frac{1}{\alpha_k^2} \frac{J_1(\alpha_k x)}{J_1(\alpha_k)} \exp\left(-\alpha_k^2 \frac{\nu t}{R^2}\right) \right]^2 x \, dx \\ &= \frac{1}{8\mu} \epsilon R^2 \cos^2\theta |\nabla\langle p\rangle_i|^2 \left[\int_0^1 4x^3 \, dx \right. \\ &\quad \left. - 32 \sum_{k=1}^{\infty} \frac{1}{\alpha_k^2 J_1(\alpha_k)} \exp\left(-\alpha_k^2 \frac{\nu t}{R^2}\right) \int_0^1 x^2 J_1(\alpha_k x) \, dx \right. \\ &\quad \left. + 64 \sum_{k=1}^{\infty} \sum_{l=1}^{\infty} \frac{1}{\alpha_k^2 J_1(\alpha_k) \alpha_l^2 J_1(\alpha_l)} \exp\left(-(\alpha_k^2 + \alpha_l^2) \frac{\nu t}{R^2}\right) \int_0^1 x J_1(\alpha_k x) J_1(\alpha_l x) \, dx \right] \\ &= \frac{1}{8\mu} \epsilon R^2 \cos^2\theta |\nabla\langle p\rangle_i|^2 \left[1 - 64 \sum_{k=1}^{\infty} \frac{1}{\alpha_k^4} \exp\left(-\alpha_k^2 \frac{\nu t}{R^2}\right) + 32 \sum_{k=1}^{\infty} \frac{1}{\alpha_k^4} \exp\left(-2\alpha_k^2 \frac{\nu t}{R^2}\right) \right] \\ &= \frac{K}{\mu} |\nabla\langle p\rangle_i|^2 \left[1 - 64 \sum_{k=1}^{\infty} \frac{1}{\alpha_k^4} \exp\left(-\alpha_k^2 \frac{\nu t}{R^2}\right) + 32 \sum_{k=1}^{\infty} \frac{1}{\alpha_k^4} \exp\left(-2\alpha_k^2 \frac{\nu t}{R^2}\right) \right]. \quad (3.4) \end{aligned}$$

At the starting time $t = 0$, the dissipation vanishes since the zeros of the Bessel function J_0 satisfy

$$\sum_{k=1}^{\infty} \frac{1}{\alpha_k^4} = \frac{1}{32}. \quad (3.5)$$

At large times, the exponential terms tend to zero and we arrive at (1.4) using Darcy’s law.

3.2. *Small- and large-time asymptotics*

In this section, we compare the small- and large-time asymptotics of the volume-averaged dissipation rate given by (2.7) and (1.4) with the exact dissipation rate. To evaluate these expressions, we need to determine the superficial velocity and the superficial acceleration. The superficial velocity can be obtained by averaging the velocity (3.2) over

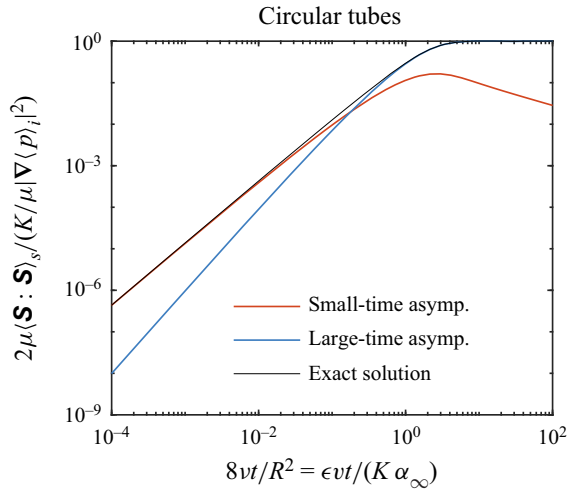


Figure 2. Comparison of the dissipation rate of the analytical solution (3.4) with the small- and large-time asymptotics (2.7) and (1.4) for a porous medium consisting of circular tubes. The dissipation is normalised with the steady-state value $K/\mu|\nabla\langle p\rangle_i|^2$.

the cross-section and then projecting it onto the direction of the pressure gradient (which amounts to a multiplication with $\cos\theta$). Using the permeability (3.1a) we get

$$\langle u \rangle_s = \frac{K}{\mu} |\nabla\langle p \rangle_i| \left[1 - 32 \sum_{k=1}^{\infty} \frac{1}{\alpha_k^4} \exp\left(-\alpha_k^2 \frac{vt}{R^2}\right) \right]. \quad (3.6)$$

By differentiation, the superficial acceleration follows as

$$\frac{d\langle u \rangle_s}{dt} = \frac{\epsilon}{\rho\alpha_\infty} |\nabla\langle p \rangle_i| \left[4 \sum_{k=1}^{\infty} \frac{1}{\alpha_k^2} \exp\left(-\alpha_k^2 \frac{vt}{R^2}\right) \right]. \quad (3.7)$$

We then evaluate the small-time asymptotics (2.7) using adaptive quadrature. Figure 2 shows the exact dissipation rate (3.4) and the small- and large-time asymptotics according to the equations (2.7) and (1.4). It can be seen that the dissipation rate is indeed well approximated by the boundary layer theory for small times and by the steady-state behaviour at large times. Note that if the superficial velocity (3.6) is substituted into the steady-state dissipation (1.4), the first two terms of the exact dissipation rate (3.4) are exactly recovered.

3.3. Evaluation of model predictions

Having demonstrated the correctness of the asymptotic limits, we can now evaluate the proposed model for the volume-averaged dissipation rate given by (2.9) and (2.11). Figure 3 shows the exact solution for the dissipation rate (3.4), the large-time asymptotics (1.4) and the modelled dissipation rate. For the blending parameter n , we have chosen the values $n = 2$ and $n = 3$ for which the predictions lie closest to the exact solution. It can be seen that the model accurately predicts the dissipation rate and has the correct limiting behaviour. The maximum relative error with respect to the instantaneous dissipation rate is 7% for $n = 2$ and 14% for $n = 3$.

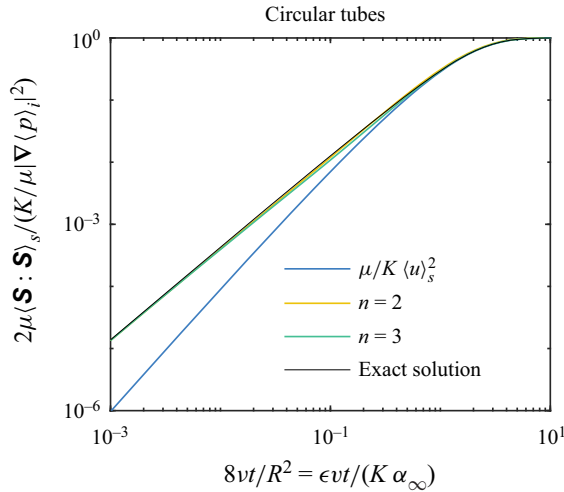


Figure 3. Comparison of the dissipation rate of the analytical solution (3.4), the large-time asymptotics (1.4) and the model given by (2.9), (2.11) for a porous medium consisting of circular tubes. The dissipation is normalised with the steady-state value $K/\mu|\nabla\langle p\rangle_i|^2$.

4. Numerical validation

In this section, we further compare the volume-averaged dissipation rate modelled according to the equations (2.9) and (2.11) with the volume-averaged dissipation rate obtained from the DNS of flow through a cylinder array and a hexagonal sphere pack.

4.1. Description of the flow solver

The simulations were performed using our in-house code MGLET (Manhart, Tremblay & Friedrich 2001). The incompressible Navier–Stokes equations are discretised on a Cartesian grid with a second-order symmetry-preserving finite volume method (Verstappen & Veldman 2003). A third-order explicit Runge–Kutta method (Williamson 1980) is employed for time integration of the momentum equation and the continuity equation is enforced using the projection method (Chorin 1968), resulting in a Poisson equation at each stage.

The no-slip and no-penetration boundary conditions at the fluid–solid interface of the porous medium are imposed using a second-order accurate ghost-cell immersed boundary method (Peller *et al.* 2006; Peller 2010). The conservation of mass in the interface cells is ensured by a flux correction procedure that is iteratively coupled to the global pressure correction. The immersed boundary method has been validated for the simulation of porous media flow in Peller (2010), Sakai & Manhart (2020) and Unglehrt & Manhart (2022).

4.2. Porous medium geometries

Following Zhu *et al.* (2014), we consider flow through a periodic array of cylinders and through a hexagonal close-packed arrangement of spheres. The corresponding simulation domains are shown in figure 4. These porous media have a considerably different porosity ($\epsilon = 0.56$ and 0.26 , respectively) and pore space geometry.

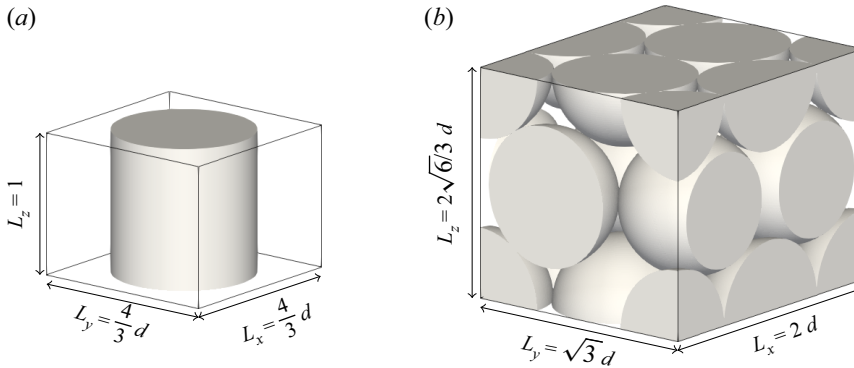


Figure 4. Simulation domains for the cylinder array and for the hexagonal sphere pack. Periodic boundary conditions are applied on all sides of the domain.

Parameter	Symbol	Cylinder array	Hexagonal sphere pack
Porosity	ϵ	$1 - (9\pi/64) = 0.5582$	$1 - (\pi/(3\sqrt{2})) = 0.2595$
Permeability	K	$5.768 \times 10^{-3} d^2$	$1.755 \times 10^{-4} d^2$
High-frequency limit of the dynamic tortuosity	α_∞	1.461	1.622
Characteristic viscous length	Λ	$0.438 d$	$5.904 \times 10^{-2} d$

Table 1. Geometric parameters for the cylinder array and the hexagonal close-packed arrangement of equal spheres.

Case	Hg	Re	Wo	Ω/Ω_0	$d/\Delta x$
cyl-step	0.1	5.74×10^{-4}	—	—	480
cyl-LF	0.1	5.72×10^{-4}	2.576	0.1	480
cyl-MF	0.1	3.62×10^{-4}	8.146	1.0	480
cyl-HF	0.1	5.08×10^{-5}	25.76	10	480
hcp-step ^a	6.5×10^1	0.0114	—	—	320
hcp-LF ^b	10^3	0.171	10	0.107	384
hcp-MF ^b	10^4	0.857	31.6	1.07	384
hcp-HF ^b	10^5	0.130	100	10.7	384

Table 2. Simulation parameters for flow through a cylinder array and a hexagonal sphere pack.

^aFrom Sakai & Manhart (2020), recomputed at a higher resolution in Unglehrt & Manhart (2023).

^bFrom Unglehrt & Manhart (2022).

The geometric parameters of these porous media are reported in table 1. The high-frequency limit of the dynamic tortuosity α_∞ and the characteristic viscous length Λ were determined from the potential flow using a finite element calculation (see Unglehrt & Manhart (2023) for the hexagonal sphere pack). The permeability values were obtained from the steady state of the simulations cyl-step and hcp-step (see table 2).

4.3. Simulation set-up

The pore scale flow is described by the incompressible Navier–Stokes equations. However, a small Reynolds number is chosen such that the nonlinear terms are insignificant.

No-slip and no-penetration boundary conditions are imposed at the cylinder or spheres and triple periodic boundary conditions are applied at the domain boundaries.

We consider flow started from rest in response to a constant pressure gradient

$$\nabla \langle p \rangle_i(t) = -g_x \mathbf{e}_x \quad \text{for } t > 0 \quad (4.1)$$

and in response to a sinusoidal pressure gradient

$$\nabla \langle p \rangle_i(t) = -g_x \sin(\Omega t) \mathbf{e}_x \quad \text{for } t > 0 \quad (4.2)$$

that are applied as a body force on the fluid. In the latter case, we have chosen three values of the frequency: $\Omega/\Omega_0 = 0.1$ (low frequency), $\Omega/\Omega_0 = 1$ (medium frequency) and $\Omega/\Omega_0 = 10$ (high frequency) where $\Omega_0 = \epsilon \nu / (\alpha_\infty K)$ is the transition frequency between the low and the high frequency regime (Pride *et al.* 1993). Note that the high-frequency cases represent behaviour that could be found, for example, in wave-induced flow in a coral reef ($d \sim 2$ cm, period ~ 4 s, wind velocity ~ 5 m s⁻¹, wave height ~ 0.6 m, water depth ~ 30 m), while the low- and medium-frequency cases would correspond to flow within a sandy seabed.

The flow cases for the cylinder array were simulated at a grid resolution of 480 cells per diameter following Zhu & Manhart (2016). The flow cases for the hexagonal sphere pack were simulated at a resolution of 384 cells per diameter for the oscillatory flow and at a resolution of 320 cells per diameter for the transient flow. They were validated by a grid study in Unglehrt & Manhart (2022) and Sakai & Manhart (2020). The important parameters of the simulations are summarised in table 2.

The time series of the volume-averaged dissipation rate was obtained indirectly from the time series of the superficial velocity and the volume-averaged kinetic energy using the kinetic energy equation (1.3),

$$2\mu \langle \mathbf{S} : \mathbf{S} \rangle_s = -\langle \mathbf{u} \rangle_s \cdot \nabla \langle p \rangle_i - \frac{d\langle k \rangle_s}{dt}. \quad (4.3)$$

The superficial velocity and the volume-averaged kinetic energy were extracted from the simulation with a high temporal resolution.

4.4. Results

We first consider the case of transient flow started from rest and driven by a constant pressure gradient. Figure 5 shows the volume-averaged dissipation rate from the DNS cyl-step and hcp-step, the large-time asymptotics (1.4) and the model evaluated for the values $n = 2$ and $n = 3$ of the blending parameter. It can be seen that the model correctly captures the small-time behaviour of the simulations whereas the dissipation rate clearly cannot be approximated by (1.4) at small times. After the first few time steps, in which the simulations are not fully accurate due to the extremely thin boundary layers, the model errors relative to the simulation lie between -18% and 4% for the cylinder array and between -12% and 8% for the hexagonal sphere pack. For the cylinder array, the blending parameter $n = 2$ gives better results, while for the hexagonal sphere pack the blending parameter $n = 3$ gives better results.

We then consider the case of transient flow started from rest that is driven by a sinusoidal pressure gradient. The low frequency cases (simulations cyl-LF and hcp-LF) are shown in figure 6. There are almost no differences between the dissipation rate of the DNS, the large-time asymptotics and the model. For the cylinder, all curves agree with the dissipation rate of the simulations. For the hexagonal sphere pack, the dissipation is

Dissipation rate model for linear unsteady porous media flow

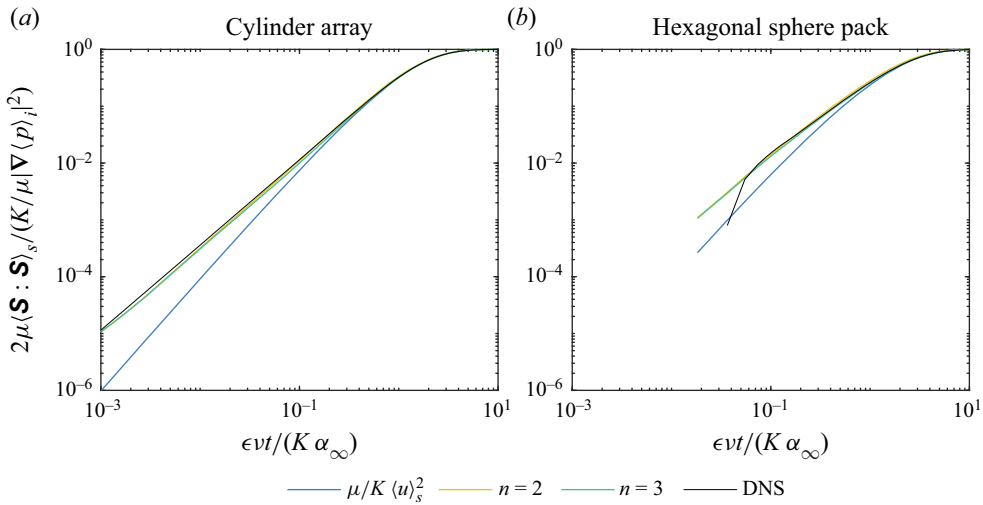


Figure 5. Comparison of the dissipation rate from the DNS, the large-time asymptotics (1.4) and the model given by (2.9), (2.11) for transient flow in response to a constant pressure gradient through the cylinder array (a) and the hexagonal sphere pack (b). The dissipation is normalised with the steady-state value $K/\mu|\nabla\langle p\rangle_i|^2$.

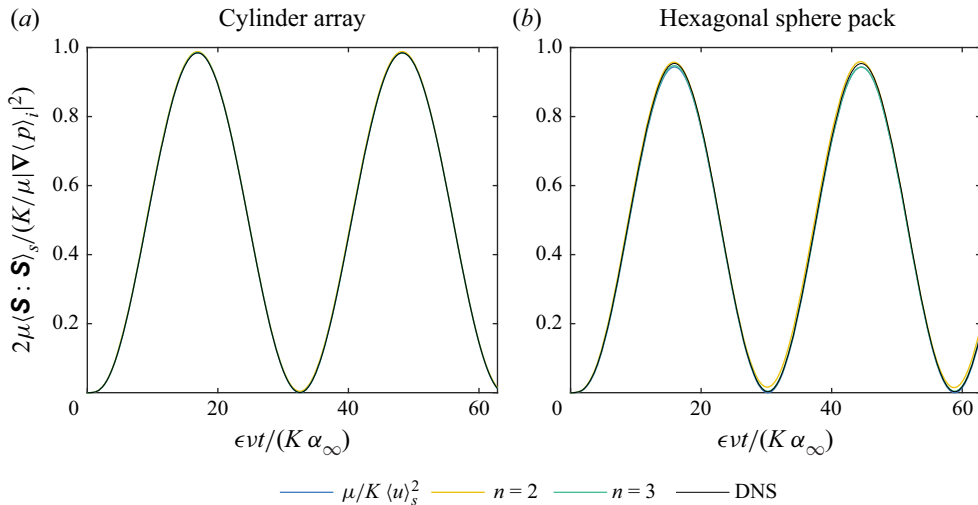


Figure 6. Comparison of the dissipation rate from the DNS, the large-time asymptotics (1.4) and the model given by (2.9), (2.11) for transient flow in response to a sinusoidal pressure gradient with $\Omega/\Omega_0 \approx 0.1$ through the cylinder array (a) and the hexagonal sphere pack (b). The dissipation is normalised with the steady-state value $K/\mu|\nabla\langle p\rangle_i|^2$.

slightly overestimated by the model for $n = 2$, while it is slightly underestimated by the model for $n = 3$ as well as by the large-time asymptotics.

The medium frequency cases (simulations cyl-MF and hcp-MF) are shown in figure 7. For the cylinder, again the large-time asymptotics agree very well with the dissipation rate of the DNS, while the model slightly overestimates the dissipation rate for both $n = 2$ and $n = 3$. For the hexagonal sphere pack, the model overestimates the dissipation rate for $n = 2$, while it is in close agreement with the simulation for $n = 3$. The large-time asymptotics slightly underestimate the dissipation rate.

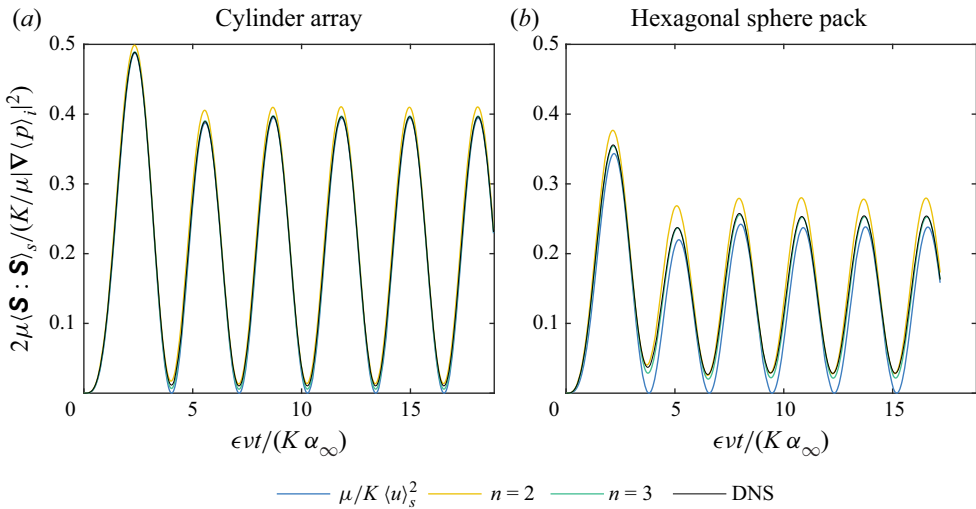


Figure 7. Comparison of the dissipation rate from the DNS, the large-time asymptotics (1.4) and the model given by (2.9), (2.11) for transient flow in response to a sinusoidal pressure gradient with $\Omega/\Omega_0 \approx 1$ through the cylinder array (a) and the hexagonal sphere pack (b). The dissipation is normalised with the steady-state value $K/\mu|\nabla\langle p\rangle_i|^2$.

The high frequency cases (simulations cyl-HF and hcp-HF) are shown in figure 8. It can be seen that the large-time asymptotics (1.4) clearly underestimate the dissipation from the simulations by approximately 30% and 55% for the cylinder array and the hexagonal sphere pack, respectively, while the model (2.9), (2.11) provides significantly better predictions. In particular, the model reproduces the evolution of the dissipation rate during the transient oscillation. For the cylinder array, a very good agreement can be observed for the value $n = 2$ of the blending parameter with a relative difference of approximately 3%; for the sphere pack, an excellent agreement between the dissipation rate from the simulation and the modelled dissipation rate is found for $n = 3$ with a relative difference of approximately 1.5%. Note that the agreement could be improved by choosing non-integer values of n . However, based on the results above, we expect that the optimal value for n will still depend on the geometry.

5. Conclusion

We have proposed a model for the volume-averaged dissipation rate in linear unsteady flow through a porous medium. The model is derived by blending the steady-state expression for the volume-averaged dissipation rate (Murthy & Singh 1997; Zhu *et al.* 2014) with a small-time asymptotic expression obtained from boundary layer theory for a flow started at rest. The model was first validated against an analytical solution of the Navier–Stokes equations for transient flow through a porous medium consisting of circular tubes. The model was then compared with a DNS dataset comprising transient and oscillatory flow through a cylinder array and through a hexagonal close-packed arrangement of spheres. The model showed significantly better predictions at small times or high frequencies than the large-time asymptotics given by the steady-state expression, while maintaining the accuracy of the large-time asymptotics at large times or low frequencies. In all cases, values of the blending parameter n between 2 and 3 gave good results.

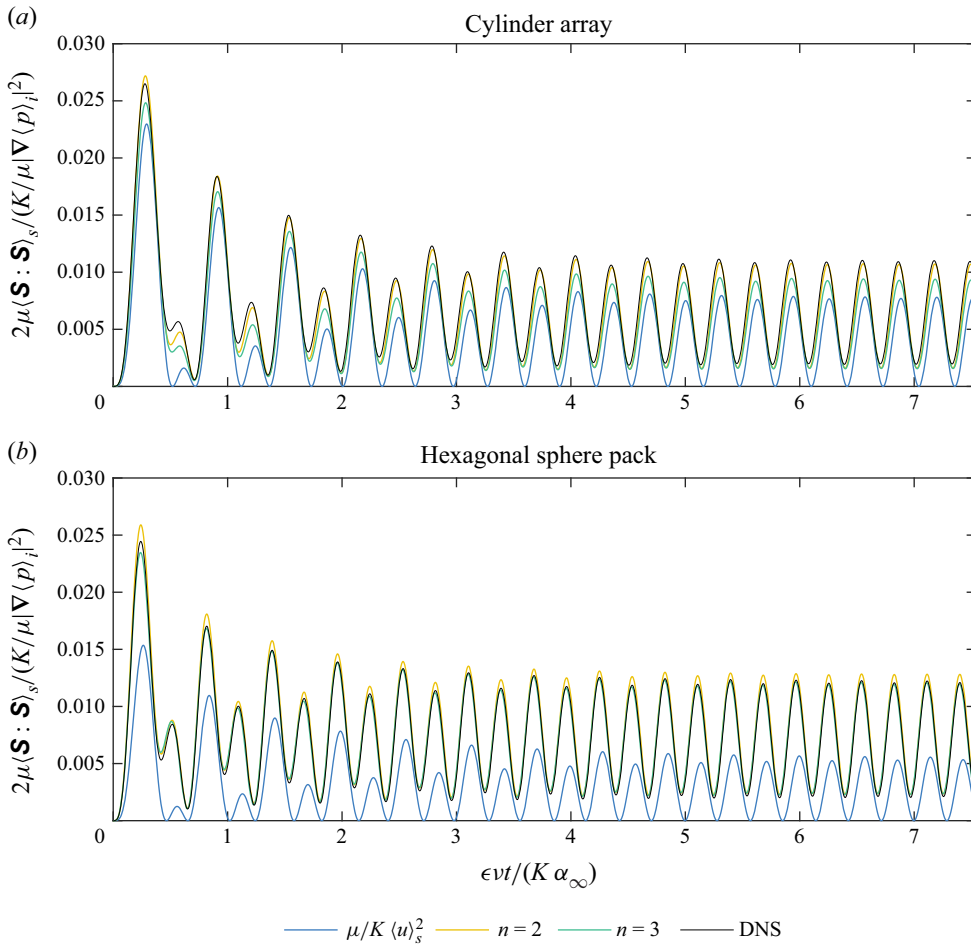


Figure 8. Comparison of the dissipation rate from the DNS, the large-time asymptotics (1.4) and the model given by (2.9), (2.11) for transient flow in response to a sinusoidal pressure gradient with $\Omega/\Omega_0 \approx 10$ through the cylinder array (a) and the hexagonal sphere pack (b). The dissipation is normalised with the steady-state value $K/\mu|\nabla\langle p \rangle_i|^2$.

Future work could attempt to generalise the model to nonlinear unsteady flow. For this, it might be promising to represent the volume-averaged dissipation rate as a Volterra series in the superficial acceleration. Furthermore, the proposed model could provide a basis for modelling dispersion and mixing in linear unsteady flow through porous media. For instance, Brosten *et al.* (2012) considered the short-time dispersion coefficient defined as $D(t) = E[|\mathbf{R}(t) - E[\mathbf{R}(t)]|^2]/(6t)$, wherein $E[\cdot]$ is the ensemble average and $\mathbf{R}(t)$ is the fluid particle displacement, and derived the following asymptotic expression for small times:

$$D(t) = D_o(t) + \left\langle (\mathbf{u} - \langle \mathbf{u} \rangle_i)^2 \right\rangle_i t + \frac{\kappa}{18} \left[\frac{\epsilon}{K} \langle \mathbf{u} \rangle_i^2 \right] t^{3/2} + O(t^{5/2}). \quad (5.1)$$

Here, $D_o(t)$ is the short-time dispersion coefficient without convection and κ is the molecular diffusion constant. The spatial velocity variance in the second term on the right-hand side is closely related to the kinetic energy and the term in brackets can be identified as the steady-state expression (1.4) in intrinsic volume-averaged form. Therefore,

within a frozen field assumption, our model allows the evaluation of these terms for unsteady linear flow.

Funding. The authors gratefully acknowledge the financial support of the Deutsche Forschungsgemeinschaft (DFG, German Research Foundation) under grant no. MA2062/13-1. Computing time was granted by the Leibniz Supercomputing Centre on its Linux-Cluster.

Declaration of interests. The authors report no conflict of interest.

Author ORCIDs.

 Lukas Unglehart <https://orcid.org/0000-0002-1299-0430>;

 Michael Manhart <https://orcid.org/0000-0001-7809-6282>.

Author contributions. L.U. derived the model, performed the simulations and wrote the manuscript. M.M. provided scientific supervision and contributed to writing the manuscript.

REFERENCES

- BATCHELOR, G.K. 2000 *An Introduction to Fluid Dynamics*. Cambridge University Press.
- BIOT, M.A. 1956a Theory of propagation of elastic waves in a fluid-saturated porous solid. I. Low-frequency range. *J. Acoust. Soc. Am.* **28** (2), 168–178.
- BIOT, M.A. 1956b Theory of propagation of elastic waves in a fluid-saturated porous solid. II. Higher frequency range. *J. Acoust. Soc. Am.* **28** (2), 179–191.
- BROSTEN, T.R. 2013 Short-time asymptotics of hydrodynamic dispersion in porous media. *J. Fluid Mech.* **732**, 687–705.
- BROSTEN, T.R., VOGT, S.J., SEYMOUR, J.D., CODD, S.L. & MAIER, R.S. 2012 Preasymptotic hydrodynamic dispersion as a quantitative probe of permeability. *Phys. Rev. E* **85** (4), 045301.
- CHA, K.S., BALARAS, E., LIEBER, B.B., SADASIVAN, C. & WAKHLOO, A.K. 2007 Modeling the interaction of coils with the local blood flow after coil embolization of intracranial aneurysms. *Trans. ASME J. Biomech. Engng* **129** (6), 873–879.
- CHAPMAN, A.M. & HIGDON, J.J.L. 1992 Oscillatory Stokes flow in periodic porous media. *Phys. Fluids A* **4** (10), 2099–2116.
- CHORIN, A.J. 1968 Numerical solution of the Navier–Stokes equations. *Maths Comput.* **22** (104), 745–762.
- CHURCHILL, S.W. & USAGI, R. 1972 A general expression for the correlation of rates of transfer and other phenomena. *AIChE J.* **18** (6), 1121–1128.
- CORTIS, A., YOUJIAN, C., SCHER, H. & BERKOWITZ, B. 2004 Quantitative characterization of pore-scale disorder effects on transport in ‘homogeneous’ granular media. *Phys. Rev. E* **70**, 041108.
- DARCY, H. 1856 *Les fontaines publiques de la ville de Dijon*. Victor Dalmont.
- ENE, H. & SANCHEZ-PALENCIA, É. 1975 Equations et phénomènes de surface pour l’écoulement dans un milieu poreux. *J. Méc.* **14**, 73–108.
- GU, Z. & WANG, H. 1991 Gravity waves over porous bottoms. *Coast. Engng* **15** (5–6), 497–524.
- JOHNSON, D.L., KOPLIK, J. & DASHEN, R. 1987 Theory of dynamic permeability and tortuosity in fluid-saturated porous media. *J. Fluid Mech.* **176**, 379–402.
- LEE, C.-Y., LEAMY, M.J. & NADLER, J.H. 2009 Acoustic absorption calculation in irreducible porous media: a unified computational approach. *J. Acoust. Soc. Am.* **126** (4), 1862–1870.
- LOWE, R.J., SHAVIT, U., FALTER, J.L., KOSEFF, J.R. & MONISMITH, S.G. 2008 Modeling flow in coral communities with and without waves: a synthesis of porous media and canopy flow approaches. *Limnol. Oceanogr.* **53** (6), 2668–2680.
- MANHART, M., TREMBLAY, F. & FRIEDRICH, R. 2001 MGLET: a parallel code for efficient DNS and LES of complex geometries. In *Parallel Computational Fluid Dynamics 2000* (ed. C.B. Jennsen, T. Kvamsdal, H.I. Andersson, B. Pettersen, A. Ecer, J. Periaux, N. Satofuka & P. Fox), pp. 449–456. North-Holland.
- MURTHY, P.V.S.N. & SINGH, P. 1997 Effect of viscous dissipation on a non-Darcy natural convection regime. *Intl J. Heat Mass Transfer* **40** (6), 1251–1260.
- NI, X., MACKLEY, M.R., HARVEY, A.P., STONESTREET, P., BAIRD, M.H.I. & RAMA RAO, N.V. 2003 Mixing through oscillations and pulsations – a guide to achieving process enhancements in the chemical and process industries. *Chem. Engng Res. Des.* **81** (3), 373–383.
- PAÉZ-GARCÍA, C.T., VALDÉS-PARADA, F.J. & LASSEUX, D. 2017 Macroscopic momentum and mechanical energy equations for incompressible single-phase flow in porous media. *Phys. Rev. E* **95** (2), 023101.

Dissipation rate model for linear unsteady porous media flow

- PELLER, N. 2010 Numerische simulation turbulenter Strömungen mit immersed boundaries. PhD thesis, Technische Universität München.
- PELLER, N., LE DUC, A., TREMBLAY, F. & MANHART, M. 2006 High-order stable interpolations for immersed boundary methods. *Intl J. Numer. Meth. Fluids* **52** (11), 1175–1193.
- POZRIKIDIS, C. 2017 *Fluid Dynamics: Theory, Computation, and Numerical Simulation*, 3rd edn. Springer.
- PRIDE, S.R., MORGAN, F.D. & GANGI, A.F. 1993 Drag forces of porous-medium acoustics. *Phys. Rev. B* **47** (9), 4964–4978.
- SAKAI, Y. & MANHART, M. 2020 Consistent flow structure evolution in accelerating flow through hexagonal sphere pack. *Flow Turbul. Combust.* **105** (2), 581–606.
- SCHLICHTING, H. & GERSTEN, K. 2017 *Boundary-Layer Theory*. Springer.
- TREVIZOLI, P.V., PEIXER, G.F. & BARBOSA, J.R. 2016 Thermal–hydraulic evaluation of oscillating-flow regenerators using water: experimental analysis of packed beds of spheres. *Intl J. Heat Mass Transfer* **99**, 918–930.
- UNGLEHRT, L. & MANHART, M. 2022 Onset of nonlinearity in oscillatory flow through a hexagonal sphere pack. *J. Fluid Mech.* **944**, A30.
- UNGLEHRT, L. & MANHART, M. 2023 Decomposition of the drag force in steady and oscillatory flow through a hexagonal sphere pack. *J. Fluid Mech.* (submitted).
- VERSTAPPEN, R.W.C.P. & VELDMAN, A.E.P. 2003 Symmetry-preserving discretization of turbulent flow. *J. Comput. Phys.* **187** (1), 343–368.
- WHITAKER, S. 1966 The equations of motion in porous media. *Chem. Engng Sci.* **21**, 291–300.
- WHITAKER, S. 1986 Flow in porous media I: a theoretical derivation of Darcy’s law. *Transp. Porous Med.* **1** (1), 3–25.
- WILLIAMSON, J.H. 1980 Low-storage Runge–Kutta schemes. *J. Comput. Phys.* **35** (1), 48–56.
- ZHU, T. & MANHART, M. 2016 Oscillatory Darcy flow in porous media. *Transp. Porous Med.* **111** (2), 521–539.
- ZHU, T., WALUGA, C., WOHLMUTH, B. & MANHART, M. 2014 A study of the time constant in unsteady porous media flow using direct numerical simulation. *Transp. Porous Med.* **104** (1), 161–179.